Modulating functionally-distinct vagus nerve fibers using microelectrodes and kilohertz frequency electrical stimulation

Author:
Qin, P; Lin, Q; Xie, Y; Chang, YC; Zanos, S; Wang, H; Payne, S; Shivdasani, MN; Tsai, D; ... Guo, T

Publication details:
Proceedings of the Annual International Conference of the IEEE Engineering in Medicine and Biology Society, EMBS
v. 00
Medium: Print
pp. 1 - 4
9798350324471 (ISBN)
1557-170X (ISSN); 2694-0604 (ISSN)

Event details:
2023 45th Annual International Conference of the IEEE Engineering in Medicine & Biology Society (EMBC)
United States
2023-07-24 - 2023-07-27

Publication Date:
2023-01-01

Publisher DOI:
https://doi.org/10.1109/EMBC40787.2023.10340796

2023 45th Annual International Conference of the IEEE Engineering in Medicine & Biology Society (EMBC) | 979-8-3503-2447-1/23/$31.00 ©2023 IEEE | DOI: 10.1109/EMBC40787.2023.10340796

Modulating functionally-distinct vagus nerve fibers using microelectrodes and kilohertz frequency electrical stimulation

Peijun Qin, *Student Member, IEEE*, Qihang Lin, Yuyang Xie, *Student Member, IEEE*, Yao-Chuan Chang, *Member, IEEE,* Stavros Zanos, *Member, IEEE,* Hao Wang, Sophie Payne, Mohit N. Shivdasani, *Senior Member, IEEE*, David Tsai, *Senior Member, IEEE*, Nigel H. Lovell, *Fellow, IEEE*, Socrates Dokos, *Member, IEEE*, Tianruo Guo, *Senior Member, IEEE*

***Abstract*— Modulation of functionally distinct nerve fibers with bioelectronic devices provides a therapeutic opportunity for various diseases. In this study, we began by developing a computational model including four major subtypes of myelinated fibers and one unmyelinated fiber. Second, we used an intrafascicular electrode to perform kHz-frequency electric stimulation to preferentially modulate a population of fibers. Our model suggests that fiber physical properties and electrode-to-fascicle distance severely impacts stimulus-response relationships. Large diameter fibers (Aα- and Aβ-) were only minimally influenced by the fascicle size and electrode location, while smaller diameter fibers (Aδ-, B- and C-) indicated a stronger dependency.**

***Clinical Relevance*— Our findings support the possibility of selectively modulating functionally-distinct nerve fibers using electrical stimulation in a small, localized region. Our model provides an effective tool to design next-generation implantable devices and therapeutic stimulation strategies toward minimizing off-target effects.**

I. Introduction

Vagus nerve stimulation (VNS) is used clinically as a treatment for a series of diseases including refractory epilepsy, depression and obesity [1]. More recent preclinical studies indicated that it could have potential therapeutic or inhibitory effects on rheumatoid arthritis [2] and inflammatory bowel disease [3]. Particularly in the cervical vagus nerve, which is the current targeted location for electrode array implantation, large, myelinated A-fibers and B-fibers convey information from primary motor neurons in the brain that control muscles or sensory neurons, convey information from muscles and joints back to the brain, and convey information regarding pain sensation [4]. Small unmyelinated C-fibers constitute the peripheral axons of sensory vagal neurons, and transmit mechanical, chemical, thermal and inflammatory signals from visceral organs to the brainstem [5]. Current VNS approaches at the cervical level indiscriminately stimulate the entire nerve bundle, resulting in considerable adverse side effects when providing therapeutic treatments [4]. For instance, when treating a patient with treatment-resistant depression, VNS can effectively shape emotional responses through recruitment of C-fibers [6]. However, it usually co-activates A- and efferent B-fibers because of their relatively low thresholds [7], causing side effects including acute apnea and cardio-inhibition [4]. Furthermore, due to off-target effects, stimulation duration and amplitude cannot reach sufficient treatment efficacy. Therefore, being able to selectively modulate these functionally distinct fibers, especially targeting C-fibers with bioelectronic devices, is expected to significantly improve therapeutic efficacy.

In addressing shortcomings of existing stimulation techniques, we conducted *in silico* investigations to explore the possibility of selectively modulating different fibers at least in a local area. We first developed a new model using the finite element method (FEM) to investigate the electrical characteristics of five types of nerve fibers. The model was validated using published electrophysiological [8-10] and histological data recorded from pig and human cervical vagus nerves [11-13]. We then used this new model to simulate fiber-specific responses to kHz frequency electrical stimulation delivered by a μm-scale penetrating nerve electrode. Finally, the influence of electrode-to-fascicle distance and stimulation amplitude on VNS performance was studied. Our model provides an effective tool to further optimize the design of VNS implants and associated electrical stimulation parameters with the aim of improving the therapeutic efficacy of VNS through selective activation of C-fibers.

II. Methodology

A. Model Geometry

All simulations were implemented in COMSOL Multiphysics v.6.0 (COMSOL Inc., Burlington, MA). Five types of fiber including Aα (diameters 13~22 μm), Aβ (diameters 6~13 μm), Aδ (diameters 1~4 μm), B (diameters 1~3 μm) and C (diameters 0.1~1 μm) [13, 14] were simulated. Physical parameters of the node, myelin and internode are listed in Table I [15, 16]. The total fiber length varied between 4489 μm and 4603 μm, depending on the myelin length. In each model fiber, the node domain was defined by a single-layer structure with a length of 1 μm. The myelin domain was defined by a double layer structure that represents myelin and internode.

The extracellular environment including nerve and fascicles were simulated as cylindrical geometries. A cross

P. Qin, Y. Xie, M.N. Shivdasani, D. Tsai, N. Lovell, S. Dokos, T. Guo are with the Graduate School of Biomedical Engineering and Tyree Institute of Health Engineering, UNSW Sydney, NSW 2052, Australia, Q. Lin is with the Comsol China, Shanghai, 200127, China. Y-C Chang is with Medtronic PLC, Minneapolis, MN, US.

S. Payne is with Bionics Institute VIC 3002 Australia, S. Zanos is with Institute of Bioelectronic Medicine Feinstein Institute for Medical Research, New York, US. H. Wang is with Shenzhen Institutes of Advanced Technology, Chinese Academy of Sciences, China

E-mail for correspondence: z5334971@ad.unsw.edu.au

section of the modelled nerve and fascicles shown in Fig. 1. The distribution and physical properties of fascicles were reconstructed based on pig histological data [11]. We explored recruitment characteristics of fibers located in three fascicles, as highlighted in Fig. 1: a (diameter 80 µm, fascicle center-electrode distance 50 µm), b (80 µm, 200 µm) and c (170 µm, 325 µm).

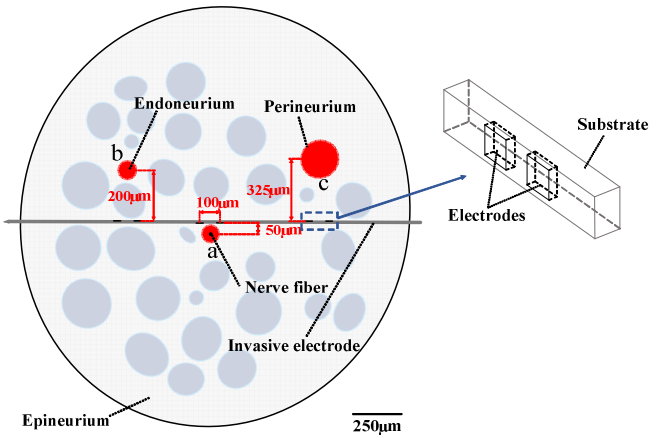

Figure 1. Reconstruction of cervical vagus nerve geometry based on pig histological data [11]. The stimulus-nerve characteristics in three fascicles a, b and c (red) were investigated. Intra-fascicular stimulation electrodes (black) were inserted via a substrate (gray), its enlargement is shown on the right.

TABLE I. MODEL GEOMETRY PARAMETERS

Type	Diameter (µm)			Length of myelin (µm)
	node	*myelin*	*internode*	
Aα-fiber	4.7	14	10.4	1500
10 µm *Aβ*-fiber	3.3	10	6.9	1150
7.3 µm *Aβ*-fiber	2.4	7.3	4.6	750
Aδ- and B-fiber	1.4	2	1.6	373.2
C-fiber	1	-	-	-

B. Model Equations for Nerve Fibers

The ion channel (i_{ion}) properties of all myelinated fibers were simulated based on the McIntyre, Richardson, Grill axon model (MRG) [15]. The unmyelinated C-fiber was simulated based on the Schwarz, Reid and Bostock axon model (SRB) [8]. The electrical properties of myelinated fibers are shown in Fig. 2.

The extracellular potential V_e was governed by Poisson's equation. The intracellular potential V_i was governed by:

$$-\nabla\left(\frac{r_i}{\rho_a}(\nabla V_i)\right) = -2C_i\left(\frac{\partial V_i}{\partial t} - \frac{\partial V_o}{\partial t}\right) - 2\frac{V_i - V_o - V_{rest}}{\frac{1}{G_i}} \quad \text{(eq.1)}$$

$$-\nabla\left(\frac{r_n}{\rho_n}(\nabla V_i)\right) + 2C_n\frac{\partial V_i}{\partial t} = -2\left(i_{ion} - C_n\frac{\partial V_o}{\partial t}\right) \quad \text{(eq.2)}$$

$$-\nabla\left(\frac{r_{my}}{\rho_p}(\nabla V_o)\right) = -2\left(C_{my}\left(\frac{\partial V_o}{\partial t} - \frac{\partial V_e}{\partial t}\right) + \frac{V_o - V_e}{\frac{1}{G_{my}}}\right) \quad \text{(eq.3)}$$

where V_o represents a virtual intermediate voltage between the internode and outer myelin layers. r_i, r_n and r_{my} denote the radii of the internode (i.e. intracellular), node, and myelin layer respectively. ρ_a, ρ_n and ρ_p represent the resistivity of the internode, node, and myelin layers respectively, whilst C_i, C_n and C_{my} denote the membrane capacitance of the internode, node and myelin layers per unit area. V_{rest} is the value of the resting potential, set to -80 mV. G_i and G_{my} denote the transverse conductance of the internode and myelin layers. Initial values of V_i and V_o were set to -80 mV and 0 mV respectively.

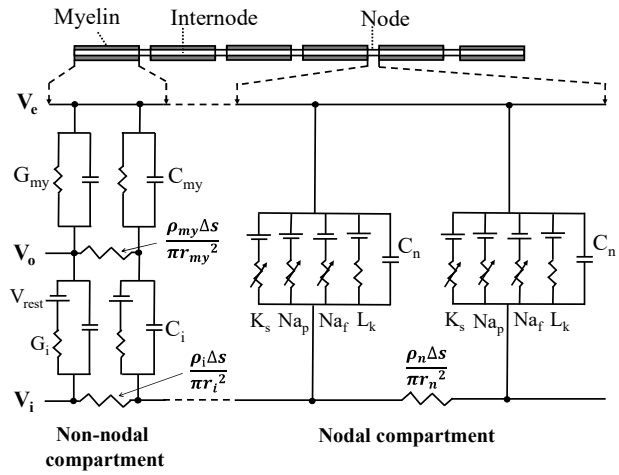

Figure 2. Electrical properties of myelinated fibers. Each modelled fiber included non-nodal and nodal compartments. Non-nodal compartments included a myelin layer (between V_e and V_o) and an internode layer (between V_i and V_o). V_o represents an intermediate voltage between the two layers.

All updated model parameters are listed in Tables I & II. Endoneurium, perineurium, and epineurium were simulated by different conductive materials with their relative permittivity set to be 1 [17, 18]. No-flux boundary conditions were used at the ends of each fiber and node segment.

TABLE II. MODEL PARAMETERS

Symbo	Description	Value
ρ_i	Internode resistivity	7.5~30 Ω·cm [a]
g_{Naf}	Maximum fast Na^+ conductance	3~3.5 S/cm^2 [b]
C_{in}	Capacitance of internode	0.03~0.05 µF/cm^2 [c]
G_i	Conductance of internode	0.0001~0.000167 S·cm^2 [d]
σ_{per}	Conductivity of perineurium	0.0021 S/m
σ_{epi}	Conductivity of epineurium	0.15873 S/m
σ_{endo_l}	Conductivity of longitudinal endoneurium	0.57143 S/m
σ_{endo_t}	Conductivity of transverse endoneurium	0.08333 S/m

a. 7.5 Ω·cm for *Aα*-fiber and 10 µm *Aβ*-fiber, 15 Ω·cm for 7.3 µm *Aβ*-fiber and 30 Ω·cm for A*δ* & B-fiber. b. 3.5 S/cm^2 for *Aα*-fiber and 10 µm *Aβ*-fiber, 3 S/cm^2 for 7.3 µm *Aβ*-fiber and A*δ* & B-fiber. c. 0.03 µF/cm^2 for *Aα*-fiber,10 µm *Aβ*-fiber and 7.3 µm *Aβ*-fiber, 0.05 µF/cm^2 for A*δ* & B-fiber. d. 0.000143 S·cm^2 for *Aα*-fiber, 10 µm *Aβ*-fiber, 0.000167 S·cm^2 for 7.3 µm *Aβ*-fiber and 0.0001 S·cm^2 for A*δ* & B-fiber. Other model parameters were set based on default MRG and SRB parameters.

C. Electrical Stimulation

As shown in Fig. 1, a pair of intra-fascicular stimulation electrodes (each 50×50 µm, with an edge-edge spacing of 50 µm) were placed on a polyimide substrate (with 2000 µm length, 70 µm width, and 10 µm thickness). In all simulations, the electrode was fixed at 1500 µm from the left boundary of the model nerve. Electrode-to-fascicle distances were set to be 50 µm, 200 µm and 325 µm for fascicles a, b and c. 8-kHz

biphasic rectangular pulses [6] at a range of amplitudes (0.1~26 mA) and 50% duty cycle were delivered to stimulate the nerve over a duration of 10-ms.

III. Results

A. Model Validation

In Fig. 3A, by delivering 20-ms suprathreshold depolarizing stimuli, the model exhibited spike frequency accommodation after 1~5 spikes [8, 10]. In addition, 2-ms hyperpolarizing current injections resulted in a hyperpolarizing afterpotential (Fig. 3B), which closely matched experimental data [9]. In Table III, the conduction velocity (CV) of modelled fibers was validated against experimental recordings from pigs [11, 12] and human [13, 14]. The CV was defined by dividing the distance between the second and last nodes by the time difference of their elicited action potentials (APs). The number of nodes for all fibers was set to 11 during the CV measurement.

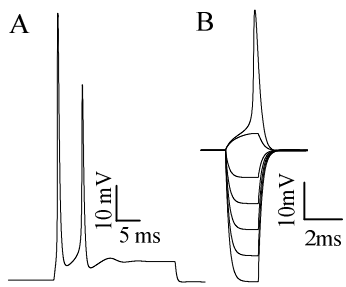

Figure 3. An example of model validation using a 10 µm $A\beta$-fiber. (A) Model response to a 20-ms suprathreshold depolarizing stimuli. (B) Model responses to multiple 2-ms hyperpolarizing current steps.

TABLE III. Conduction Velocity of Fibers

Type	Model	Biological Recording
$A\alpha$-fiber	70.59 m/s	>33 m/s[11] or 70~120 m/s[13]
10 µm $A\beta$-fiber	57.5 m/s	>33 m/s[11] or 35~75 m/s[14]
7.3 µm $A\beta$-fiber	35.29 m/s	>33 m/s[11] or 35~75 m/s[14]
$A\delta$ and B -fiber	8.91 m/s	<25 m/s[11] or 3~15 m/s[13]
C-fiber	0.6818 m/s	<5 m/s[12] or 0.2~2 m/s[13]

B. Single Fiber Activities under 8-kHz Stimulation

In all single fiber stimulation models, a fiber was located at the center of a fascicle. In Fig. 4A, all myelinated fibers exhibited a non-monotonic stimulus-amplitude-dependent response to an 8-kHz pulse train. However, leveraging the biophysical differences across fibers, different fibers demonstrated unique stimulus-response characteristics. For example, with smaller fiber diameters, myelinated fibers exhibited an increased threshold and a decreased slope of the rising phase (the phase in which spike counts increase with increasing stimulation current) and concomitantly, an earlier onset of the falling phase (in which the total spike numbers saturate or decline). In contrast, unmyelinated C-fibers only exhibited a rising phase in the given stimulus range. This trend also occurred in fibers from other simulated fascicles with different sizes and electrode-to-fascicle distances (Fig. 4B and C). In addition, the myelinated-unmyelinated selectivity index (defined by the ratio of C-fiber threshold and Aδ- & B-fiber blocking intensity) increased from 13 in fascicle a, to 85 in fascicle c (results not shown since the thresholds were out of given stimulus range in fascicle c).

C. Population-based Simulation

To simulate the influence of electrode-to-fiber distances in VNS performance, we added multiple myelinated fibers in nerve fascicle b. In Fig. 5, each fiber was locally defined using a 2D coordinate system in which the center of the fascicle acted as the origin (0, 0). Five fibers were placed at (0 µm, 0 µm), (0 µm, 30 µm), (0 µm, -30 µm), (30 µm, 0 µm) and (-30 µm, 0 µm). Our population-based simulation also suggested a fiber-specific stimulus intensity window for excitation and blocking. In contrast to single fiber stimulation in Fig. 4, certain blocked smaller myelinated fibers (2 µm Aδ- & B-fibers, 8~25 mA) could be re-activated with high current when they were located relatively far from the electrodes, agreeing with previous modelling studies [19]. In addition, all C-fibers in nerve fascicle a exhibited sustained activation at 25 mA.

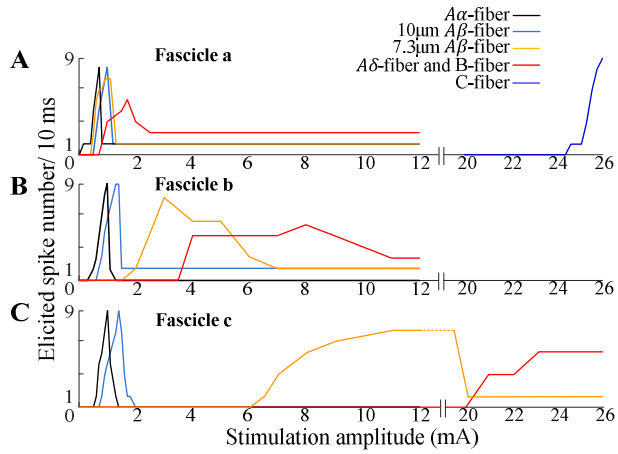

Figure 4. Recruitment characteristics of functionally-distinct fibers in fascicles a, b and c under 8-kHz frequency stimulation. In each fascicle, smaller fibers showed larger activation thresholds and blocking onsets. By increasing electrode-to-fascicle distances, the stimulus intensity values of activation and blocking for all fibers increase, especially for relatively smaller fibers. The elicited C-fiber activities in fascicles b and c were not shown because their thresholds were out of the given stimulus intensity window.

IV. Discussion and Conclusion

The model presented here represents the first step toward accurate cervical vagus nerve fiber modeling encompassing all major nerve fiber types [11, 13]. It accurately reconstructed detailed nerve physical properties including fascicular structure, perineurium, endoneurium, and epineurium based on biological data in pigs [11, 20] and humans [17, 18, 21]. It also included an intra-fascicular microelectrode to simulate close juxtaposition to nerve fibers, enabling focal stimulation at the µm-scale. Finally, the optimized model was used to predict performance of penetrating microelectrodes under kHz-frequency electrical stimulation.

Our simulations suggested that fiber physical properties and electrode-to-fascicle distance can shape stimulus-response relationships (Figs. 4 and 5). In each fascicle, fiber diameter was negatively correlated with activation threshold and blocking onset. Increasing the fascicle size and electrode-to-fascicle distance did not qualitatively change the above fiber-specific relationships but increased the stimulus intensity values of activation and blocking for all fibers. Notably, the large diameter fibers ($A\alpha$- and $A\beta$- fibers) were only minimally influenced while smaller diameter fibers ($A\delta$-, B-

and C-fibers) indicated a stronger dependency of the fascicle size and location. These results indicated a preferred stimulus parameter space for modulating the activity of different fibers.

In Fig. 4C, when the electrode-to-fascicle distance was increased to 325 µm, Aδ- and B-fibers could not be blocked over the given stimulus intensity window, suggesting a physical limit of blocking myelinated fibers with a "single-line" electrode array, where functionally selective activation is no longer possible. These simulations provide theoretical evidence on the basis of which sophisticated electrode array geometries for improved selectivity can be designed. Fig. 5 indicates the possibility of population-based myelinated-unmyelinated selectivity. Functionally distinct myelinated fibers demonstrated their unique parameter space for blocking. 25 mA pulses displayed the ability to selectively activate small diameter unmyelinated C-fibers in a local region, indicating therapeutic benefits in treatment of a range of disease conditions while minimizing multiple side effects [4].

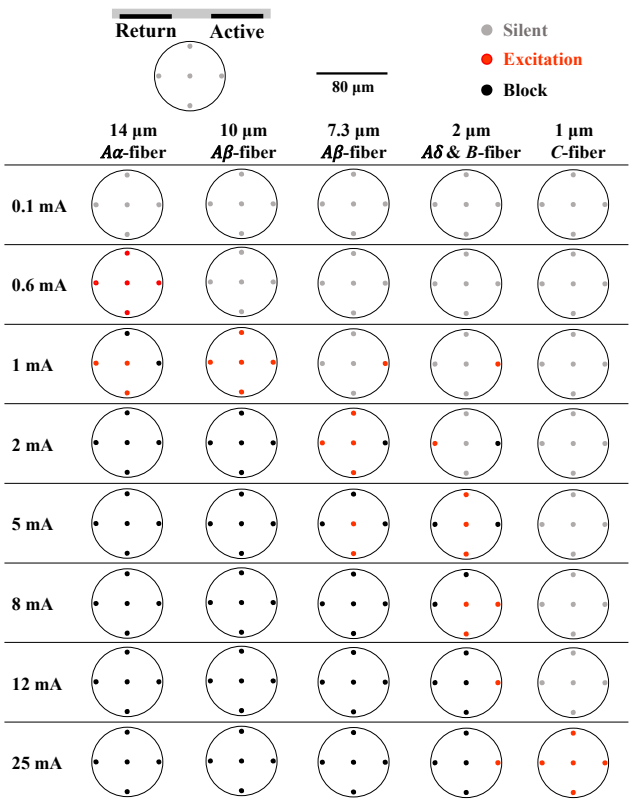

Figure 5. Population-based conduction responses across different fiber subtypes and current amplitudes. Three fiber activities were chosen. Silent: subthreshold activity. Excitation: electrically elicited spiking activities. Block: suprathreshold inhibition activities reducing spikes to ≤ 2. At 0.1 mA, all fibers were silent. Between 0.6 mA and 8 mA, a population of fibers with decreasing diameters was activated sequentially and then blocked. After 8 mA, certain Aδ- & B-fibers started being re-activated. C-fibers in a local region became excitable after 25 mA.

In summary, this study suggests a new neuromodulation approach that can block myelinated fibers while activating unmyelinated fibers. Our previous *in vivo* study has used A-fiber associated electromyography, B-fiber associated heart rate, and C-afferent-fiber associated breathing interval to estimate the electrically-elicited selectivity [4]. One major step closer to achieving more clinically relevant stimulation will be validating the model predictions using *in vivo* animal models. Adding more detailed anatomical microstructures [11, 17, 21] and fiber distribution [11] will also improve the biological features of this model.

References

[1] C. W. Austelle, G. H. O'Leary, S. Thompson, E. Gruber, A. Kahn *et al.*, "A comprehensive review of vagus nerve stimulation for depression," *Neuromodulation,* vol. 25, no. 3, pp. 309-315, 2022

[2] R. L. Johnson and C. G. Wilson, "A review of vagus nerve stimulation as a therapeutic intervention," *J Inflamm Res,* vol. 11, pp. 203-213, 2018

[3] Y. Mikami, J. Tsunoda, H. Kiyohara, N. Taniki, T. Teratani *et al.*, "Vagus nerve-mediated intestinal immune regulation: therapeutic implications of inflammatory bowel diseases," *Int Immunol,* vol. 34, no. 2, pp. 97-106, 2022

[4] U. Ahmed, Y. C. Chang, S. Zafeiropoulos, Z. Nassrallah, L. Miller *et al.*, "Strategies for precision vagus neuromodulation," *Bioelectron Med,* vol. 8, no. 1, p 9, 2022

[5] S. L. Prescott and S. D. Liberles, "Internal senses of the vagus nerve," *Neuron,* vol. S0896-6273(21)01037-0, 2022

[6] Y. C. Chang, U. Ahmed, N. Jayaprakash, I. Mughrabi, Q. H. Lin *et al.*, "kHz-frequency electrical stimulation selectively activates small, unmyelinated vagus afferents," *Brain Stimul,* vol. 15, no. 6, pp. 1389-1404, 2022

[7] R. M. McAllen, A. D. Shafton, B. O. Bratton, D. Trevaks, and J. B. Furness, "Calibration of thresholds for functional engagement of vagal A, B and C fiber groups in vivo," *Bioelectron Med,* vol. 1, no. 1, pp. 21-27, 2018

[8] J. R. Schwarz, G. Reid, and H. Bostock, "Action potentials and membrane currents in the human node of Ranvier," *Pflugers Arch,* vol. 430, no. 2, pp. 283-92, 1995

[9] A. R. Blight and S. Someya, "Depolarizing afterpotentials in myelinated axons of mammalian spinal cord," *Neuroscience,* vol. 15, no. 1, pp. 1-12, 1985

[10] M. Baker, H. Bostock, P. Grafe, and P. Martius, "Function and distribution of three types of rectifying channel in rat spinal root myelinated axons," *J Physiol,* vol. 383, pp. 45-67, 1987

[11] N. Jayaprakash, W. Song, V. Toth, A. Vardhan, T. Levy *et al.*, "Organ- and function-specific anatomical organization and bioelectronic modulation of the vagus nerve," *Brain Stimul,* vol. 16, no. 2, pp. 484-506, 2022

[12] B. W. Metcalfe, T. N. Nielsen, N. D. Donaldson, A. J. Hunter, and J. T. Taylor, "First demonstration of velocity selective recording from the pig vagus using a nerve cuff shows respiration afferents," *Biomed Eng Lett,* vol. 8, no. 1, pp. 127-136, 2018

[13] J. L. Parker, N. H. Shariati, and D. M. Karantonis, "Electrically evoked compound action potential recording in peripheral nerves," *Bioelectron. Med,* vol. 1, no. 1, pp. 71-83, 2018

[14] H. Yuan and S. D. Silberstein, "Vagus nerve and vagus nerve stimulation, a comprehensive review: part I," *Headache,* vol. 56, no. 1, pp. 71-8, 2016

[15] C. C. McIntyre, A. G. Richardson, and W. M. Grill, "Modeling the excitability of mammalian nerve fibers: influence of afterpotentials on the recovery cycle," *J Neurophysiol,* vol. 87, no. 2, pp. 995-1006, 2002

[16] C. C. McIntyre, W. M. Grill, D. L. Sherman, and N. V. Thakor, "Cellular effects of deep brain stimulation: model-based analysis of activation and inhibition," *J Neurophysiol,* vol. 91, no. 4, pp. 1457-69, 2004

[17] Y. Grinberg, M. A. Schiefer, D. J. Tyler, and K. J. Gustafson, "Fascicular perineurium thickness, size, and position affect model predictions of neural excitation," *IEEE Trans Neural Syst Rehabil Eng,* vol. 16, no. 6, pp. 572-81, 2008

[18] N. A. Pelot, C. E. Behrend, and W. M. Grill, "On the parameters used in finite element modeling of compound peripheral nerves," *J Neural Eng,* vol. 16, no. 1, 2019

[19] N. A. Pelot, C. E. Behrend, and W. M. Grill, "Modeling the response of small myelinated axons in a compound nerve to kilohertz frequency signals," *J Neural Eng,* vol. 14, no. 4, p 046022, 2017

[20] M. L. Settell, N. A. Pelot, B. E. Knudsen, A. M. Dingle, A. L. McConico *et al.*, "Functional vagotopy in the cervical vagus nerve of the domestic pig: implications for the study of vagus nerve stimulation," *J Neural Eng,* vol. 17, no. 2, p 026022, 2020

[21] N. A. Pelot, G. B. Goldhagen, J. E. Cariello, E. D. Musselman, K. A. Clissold *et al.*, "Quantified morphology of the cervical and subdiaphragmatic vagus nerves of human, pig, and rat," *Front Neurosci,* vol. 14, p 601479, 2020